Direct observation of two-step crystallization in nanoparticle superlattice formation

Jungwon Park[1,2], Haimei Zheng[2], Won Chul Lee[3], Phillip L. Geissler[1,4], Eran Rabani[5], and A. Paul Alivisatos[1,2]*

[1] Department of Chemistry, University of California, Berkeley, CA, 94720, USA

[2] Materials Sciences Division, Lawrence Berkeley National Laboratory, Berkeley, CA, 94720, USA

[3] Department of Mechanical Engineering, University of California, Berkeley, CA, 94720, USA

[4] Chemical Sciences Division, Lawrence Berkeley National Laboratory, Berkeley, CA, 94720, USA

[5] School of Chemistry, The Sackler Faculty of Exact Sciences, Tel Aviv University, Tel Aviv, 69978, Israel

* e-mail: APAlivisatos@lbl.gov

Abstract

Direct imaging of nanoparticle solutions by liquid phase transmission electron microscopy has enabled unique in-situ studies of nanoparticle motion and growth. In the present work, we report on real-time formation of two-dimensional nanoparticle arrays in the very low diffusive limit, where nanoparticles are mainly driven by capillary forces and solvent fluctuations. We find that superlattice formation appears to be segregated into multiple regimes. Initially, the solvent front drags the nanoparticles, condensing them into an amorphous agglomerate. Subsequently, the nanoparticle crystallization into an array is driven by local fluctuations. Following the crystallization event, superlattice growth can also occur via the addition of individual nanoparticles drawn from outlying regions by different solvent fronts. The dragging mechanism is consistent with simulations based on a coarse-grained lattice gas model at the same limit.

Main text

Nanoparticles (NPs), also known as artificial atoms, provide an ideal model system to study crystallization at the nanometer scale and above. This is because their physical properties can be tuned by changing their composition, size, and surface ligand, allowing for control over the interparticle interactions.[1] This offers an opportunity to uncover the interplay between entropic and enthalpic effects in the self-assembly process and perhaps, provide the necessary insights that would help guide the creation of large scale arrays suitable for future energy harvesting and optoelectronic device applications that rely on the bottom-up approach.[2,3] Understanding the phase behavior of colloidal NP solutions from dispersions to two- and three-dimensional solids has considerable fundamental and practical importance.[4,5]

Most NP assemblies, however, are formed under empirically optimized, perhaps uncontrolled, drying conditions. Experimental studies of the fundamental mechanisms of assembly formation are very desirable since the final morphologies are very sensitive to different crystallization conditions including size, shape, solubility and surface ligand of the NPs, the evaporation rate of the solvent, inter-particle interactions, and particle-substrate interactions.[6-13] The lack of such studies is even more notable in view of recent theoretical progress based on the Dzyaloshinskii-Lifshitz-Potaevskii model, the coupled-dipole method, and the coarse-grained lattice-gas models.[1,14] These have sought to explain how interactions

among NPs and solvent fluctuations affect final assembled structures, yet many of the predictions await experimental assessment.

In-situ optical microscopy was used successfully to quantify the real time and real space crystallization and melting of colloidal polystyrene microshperes, providing great insight into the forces between the particles and the factors influencing crystallization and melting.[15-21] In NP assembly, where the size domain is below the diffraction limit of visible light, in-situ atomic force microscopy, optical microscopy, and small angle X-ray scattering have been the leading tools to study the nucleation and growth of NP clusters and the formation of superlattices at liquid/air and liquid/substrate interfaces.[6,22-25] However, microscopic details of how single NPs position at potential lattice points of a growing superlattice remain elusive. With the recent development of in-situ liquid cells for transmission electron microscopy (TEM), it is now possible to extend these studies down to the nanoscale.[26-28]

In this work, we employed liquid-phase TEM and observed the formation of Pt NP assemblies, in-situ, at the substrate/solvent/vacuum interface. The technique provides means to follow individual NP trajectories and to study in depth the evolution of the system to an ordered assembled state in real time. We demonstrate that during assembly, Pt NPs were mainly driven by the strong capillary force of the evaporating solvent front. We find that the assembly proceeds by several distinct steps. In the first, NPs are contracted and condensed by the rapidly moving solvent into amorphous agglomerates, which span several monolayers in thickness. These agglomerates then expand and flatten to a single NP thickness. At this point, local

fluctuations allow the system to relax to an ordered superstructure. These domains then grow by the subsequent addition of NPs, where capillary forces play an important role as well. Coarse-grained modeling provides a consistent picture with these experiments.

Pt NPs with 7.3 nm average diameter were synthesized by the reduction of ionic Pt precursors and dispersed in a 1:4 pentadecane: o-dichlorobenzene mixture with a small amount of oleylamine added in (see Methods for more detail).[29] The NP solution was then loaded into the liquid cell reservoirs and the liquid cell was airtight for in-situ TEM observation. Such procedure provides approximately 30 minutes of viewing time. A schematic diagram of the liquid cell can be found in previous reports supporting information (SI).[28,30] Figure 1 summarizes the NP assembly formation obtained from a typical in-situ liquid TEM experiment (see also Movie 1). The electron beam has been used not only as an imaging tool but also as a driving force to evaporate the solvent locally from the illuminated area. Varying solvent thicknesses induced by the electron beam radiation can be seen as change in contrast as time progresses with thinner areas appearing as lighter contrast and thicker areas appearing as darker contrast (Fig 1a). Solvent evaporation nucleates at several spots which show up as bright circles in the first image and continue to expand until the solvent is gone in the final image. Similar patterns were observed during the evaporation of water.[31] We also tracked several NPs forming one large domain in the final stage. Their relative positions (corrected for thermal drift of the TEM – see SI for more details), corresponding to the red-squared area in the TEM images, are shown in Fig. 1b, Fig. S2, and Movie 2.

It is important to note that the length scale of the final ordered assembly is limited by the observation process, and the fact that evaporation is initiated at multiple independent sites. Nonetheless, we can track the motion of every particle associated with one evaporation zone, and in this way decipher the critical steps of NP assembly. Assembly driven by a single larger evaporation front, such as often occurs by ordinary evaporation in lab experiments outside the TEM, would likely follow the same microscopic steps, and further evidence for this will be shown below.

The motion of the NPs was captured with camera frame speeds of five to thirty frames per second, in order to track individual NPs with adequate precision. The thickness of the liquid sample with NPs was limited to less than 100nm. Under the current experimental setup, the NP Brownian motion was significantly suppressed. The gap between two SiNx windows was controlled by the height of indium spacer during fabrication steps but the actual thickness of the liquid sample could be thinner than the desired gap size, since excess solvent (o-dichlorobenzene) was dried during the sample loading. In this regime, the NPs motion is mainly determined by the formation of drying patches. As the drying patches expand, solvent fronts push the NPs to areas that are still wet by the solvent (Fig. 1a and Movie 1). The inter-particle distance continuously decreases until NPs eventually pack together in an ordered 2D phase (Figs. 1a and 1b).

This picture is also consistent with lattice-gas simulation results shown in Fig. 1c (see also Fig. S4 and Fig. S5) under low NP diffusivity, where in addition to diffusive

motion, NPs can also move as a result of solvent dragging (complete description of the lattice gas model and the dynamics is explained in Methods below, SI, and previous reports).[14,32-34] The results shown in Fig. 1c illustrate several important points. In the limit where the self-assembled structures are determined by solvent fluctuations, dragging can provide a competing mechanism for NP assembly, even when the NP diffusivity is rather low. The resemblance between the final morphologies obtained here and our previous simulations which ignored dragging (not shown)[33] is rather striking (see also Fig. 3 for the experimental comparison). Despite the fact that in the absence of evaporation the NPs' mean square displacement (MSD) is quite low, dragging can move the NPs on length- and time-scales relevant for self-assembly, moving the particles across the detection window as they meet to form an ordered domain. The correlation between the morphologies obtained by the TEM experiments and the coarse-grained simulations further supports the importance of solvent dragging.

For each frame in Fig. 1a, we selected 51 NPs (same particles as in Fig. 1b) forming one large domain at the final assembly stage and calculated their two-dimensional projected surface coverage within the minimum convex polygonal area containing all the selected NPs. In Fig. 2 we show typical coverage plots corresponding to the trajectory shown in Fig. 1b. The behavior of the surface coverage of NPs can be divided into four regimes (1st: 0 sec to 20 sec, 2nd: 20 sec to 40 sec, 3rd: 40 sec to 58 sec, and 4th: 58 sec to 68.7 sec). In the first stage, the inter-particle distance decreases as NPs are dragged together by the evaporating solvent front. However,

the rate of evaporation is retarded due to capillary condensation in the second stage. As the inter-particle distance decreases, the solvent trapped between NPs exposes less surface to the atmosphere and evaporates more slowly.[14,34] This leads to a retarded evaporation rate resulting in a slower increase of density in the second stage. During the third stage, density reaches its maximum level which indicates that the NPs have condensed, containing multiple layers of NPs. Upon completion of evaporation in the fourth regime, these multiple layers flatten out into ordered domains while maintaining maximum level of surface coverage. During the very last stage of assembly formation, solvent fluctuations compress the NPs onto the substrate to form a stable superlattice as the solvent dries completely.

In Fig. 2 we also plot the 2D bond orientational order parameter as a function of time for the same trajectory to quantify crystalline ordering of the selected NPs.[17,20,35,36] The bond orientational order parameter is defined by:

$$\Psi_6 = \left| \langle \frac{1}{nn} \sum_{k=1}^{nn} \exp\left(6i\theta_{jk}\right) \rangle \right|$$

where $\theta_{jk}$is the angle of the bond between particle *j* and its neighbor *k*, and *nn* is the number of nearest neighbors. Nearest neighbors were defined as NPs whose inter-particle separation fell below a cutoff value that was derived from the first minimum of the radial distribution function (Fig. S3).[20] The value of Ψ_6 is 1 for an ordered structure on a triangular lattice and near 0 for a disordered lattice. Ψ_6 shows a small fluctuation before it abruptly spikes up around 57 sec to a value of ~0.5. The maximum value of Ψ_6 at the final stage is lower than 1 due to finite size effects. The most interesting observation is the abrupt increase of Ψ_6 that occurs after the

density of NPs plateaus (58 sec). This indicates that NPs form a very dense amorphous structure before crystallization. This is consistent with a two-step crystallization mechanism observed in nucleation of protein and micro-sized colloidal particles, where monomers first form an amorphous dense phase followed by crystallization.[5,37-40] A similar two-step crystallization process has been demonstrated for the self-assembly of binary mixtures within a coarse-grained model.[41]

Once under view in the TEM, the 200 kV electron beam radiation interacts strongly with the liquid.[42] One effect we see clearly is beam-induced evaporation. Thus, a concern one may raise is related to the effects of the electron beam and TEM conditions on the self-assembly process. As a check, we have also compared the final assembled domain with superlattice structures formed by drop-casting on a SiNx membrane TEM grid. The SiNx membrane was prepared by the exact same fabrication process as for the SiNx windows of a liquid cell to ensure substrate interaction effects are identical. Figure 3 compares final domains from assemblies formed under electron beam irradiation and typical superlattice patterns resulting from a drop-casting experiment (see also Fig. S6 for simulated superlattice patterns with different coverage). Localized and heterogeneous drying condition in TEM due to the presence of the electron beam results in a smaller length scale and less uniformity of the superlattice formed in the TEM compared to the drop-casting experiment. However, beyond similarity between overall superlattice patterns for the two cases, the identical inter-particle distance indicates that the slightly overlapping NP ligand shells remain intact (Fig. S3).

We find that individual NPs follow different pathways to their ordered positions in the final assembled domain. Trajectories of selected NPs from Fig. 1b and their MSD are shown in Fig. 4a and 4b. Some NPs, labeled by scaled orange color, are continuously dragged by the solvent throughout the assembly formation in a small distance scale compared to the average MSD for the selected 51 NPs (green line). Other NPs, labeled by scaled blue color, follow a different pathway. They are dragged by the solvent at the beginning until they agglomerate into a sparse amorphous structure. Local fluctuations and further drying drives the NPs into their final ordered structure, as indicated by the decline in the slope of the MSD. Simulated trajectories in Fig. 4c also show that individual NPs dragged by the solvent front follow different pathways. Three NPs that show distinct dynamics are enlarged and marked in red, brown, and blue squares. The blue NP is carried across a large distance by the solvent front, while the other NPs cover a relatively small distance. In addition, depending on how the solvent front recedes, NPs that are close to each other at early times before assembly occurs (red and brown squares) can end at quite different locations in the assembled domain. The individual NP trajectories are not only affected by the capillary forces imposed by the solvent but also by local fluctuations that lead to distinct dynamics for individual NPs.

In previous studies, convective transport of microparticles by capillary forces was found to be a main factor governing growth of domains as well as nucleation.[15,43] In Fig. 5 (see also Movie 3) we show that this indeed is the case here as well. NPs first

form small ordered domains. These domains then grow by the addition of individual NPs, where a freely moving NP, marked with an arrow, adds to an ordered array of NPs. The left column displays TEM images and the right column the corresponding images with a rainbow color overlay to clarify the solvent boundary and dried areas. The color scheme shows the white areas as low contrast regions due to drying of the solvent. Over the entire observation time NPs in the ordered array are blinking which indicates the rapid changes in their crystal orientation, demonstrating that they are still in wet conditions. The tagged NP approaches the array and fluctuates continuously upon contact until it fills the vacancy. While in ordinary nucleation theory the mobility of single particles is Brownian-like, in the present case, it seems to be coupled strongly with the drying vapor front.

In-situ liquid cell TEM observation is the only method we know of that can offer the types of trajectories shown here, so it is desirable to determine if there are other additional effects besides evaporation that the beam could have on the sample. Possible effects include mechanical momentum transfer, atomic displacement, bond breakage, heating, radiolysis, and charging amongst numerous others.[42] We see no strong evidence that any of these processes alter the trajectories. We have calculated the beam induced heating and it is very small.[30] We have calculated the degree of momentum transfer and it too is very small.[30] It is more difficult to make any definitive statements regarding chemical changes induced by the beam. There is no question that the e-beam could be chemically perturbative, and it will require substantial more study to fully establish if this is happening. The close similarity in the final structures between those observed here and those obtained by standard

evaporation techniques shows that at least the e-beam does not change the final outcome of the assembly process.

In this paper, we used a liquid phase TEM to image the drying-mediated self-assembly of NPs in real time. As the solvent evaporates under electron beam irradiation, NPs are dragged by the receding solvent front to form an ordered superlattice array. The superlattice formation is composed of several steps and actual crystallization takes place after the NPs are contracted into a dense disordered phase. In addition, domains can continue to grow by the addition of NPs that are dragged by capillary forces. Lattice gas simulation results provide a consistent picture when the motion of NPs is governed by solvent fluctuations and capillary forces rather than Brownian motion. Our work provides experimental tools needed to better understand the mechanisms of drying-mediated self-assembly at the level of single NP dynamics.

Methods

Synthesis of Pt nanoparticles and preparation of liquid cell sample. Pt NPs were prepared by following previously reported method with modification.[29] A total of 0.05 mmol of Pt ions ((NH4)2Pt(IV)Cl6: 80% and (NH4)2Pt(II)Cl4: 20%), 0.75 mmol of tetramethylammonium bromide, and 1.00 mmol of poly(vinylpyrrolidone) (in terms of the repeating unit; *M*w 29 000) were dissolved into 10 mL of ethylene glycol in a 25 mL round-bottom flask at room temperature. This solution was heated to 180 °C in an oil bath at 60 °C/min and kept at 180 °C for 20 min under argon flow and magnetic stirring. After formation of dark brown solution, it was cooled to room temperature. Acetone (90 mL) was added and black suspension was separated by centrifugation at 3000 rpm for 10 min. The black product was re-dispersed in 20 mL of ethanol and precipitated by adding excess amount of hexane. This cleaning process was repeated two or three times. Resulting Pt NPs were dispersed in excess amount of oleylamine for further ligand exchange reaction and refluxed overnight in an oil bath under mild stirring. NPs were separated from the solution by centrifugation at 14000 rpm for 30 min. Obtained Pt NPs were soluble in organic solvents. For in-situ liquid cell experiment, here, Pt NPs were dispersed in organic solvent mixture (*o*-dichlorobenzene : pentadecane : oleylamine = 100 : 25 : 1 in volume ratio). As-prepared Pt NPs solution in solvent mixture was loaded into two reservoirs of liquid cell by micro-pipette. Liquid sample was exposed ambient condition for a while to ensure that *o*-dichlorobenzene dries out before sealing. Vacuum grease was applied on one side of copper aperture grid with a hole size of

600 micrometers. Liquid cell was covered with vacuum grease applied aperture grid for airtight environment.

Coarse-grained lattice gas simulation. Simulations have been performed in 3D with a lattice gas Hamiltonian defined by:

$$H = -\varepsilon_\ell \sum_{ij} \ell_i \ell_j - \mu \sum_i \ell_i - \varepsilon_n \sum_{ij} n_i n_j - \varepsilon_{n\ell} \sum_{ij} n_i \ell_j - \varepsilon_{\ell s} \sum_{ij} \ell_i s_j - \varepsilon_{ns} \sum_{ij} n_i s_j,$$

where the sums run only over nearest neighbors on a rectangular 3D lattice, ℓ_i, n_i, and s_i are binary variables roughly proportional to the density of the solvent, NPs and substrate at site i, respectively (0 for low density or 1 for high density). ε_ℓ, ε_n, $\varepsilon_{n\ell}$, $\varepsilon_{\ell s}$, and ε_{ns} are the liquid-liquid, NP-NP, liquid-NP, liquid-substrate, NP-substrate interfacial energies, respectively, and μ is the chemical potential (for more details, see references.).[14,32-34] The dynamics are stochastic both for solvent density fluctuations and for NP diffusion, where balance is preserved. The NPs undergo a random walk on the lattice, biased by their interactions. We attempt to displace a NP by single lattice spacing in a random direction every N_ℓ solvent moves (defined below), but only if the region into which the NP moves is completely filled with liquid. To mimic the low mobility of NPs we choose a large value for N_ℓ (typically 3 orders of magnitude larger than our previous simulations). Such a move is accepted with the Metropolis probability $P_{acc} = \min[1, \exp(-\beta \Delta H)]$, where β is the inverse temperature and ΔH is the energy difference between the new and old configuration. Liquid moves are more evolved to include, in a primitive way, "dragging" of the NPs

by the receding solvent front. We attempt to convert a randomly chosen lattice cell i_{rnd} occupied by the solvent ($\ell_{i_{rnd}} = 1 \rightarrow 0$), but only if at least one of the adjacent lattice cells contains vapor. In addition, if at least one of the neighboring cells is occupied by NPs, we attempt to "drag" the NP in the opposite direction of the cell i_{rnd} with a probability ξ (i.e. not every evaporation move includes a dragging attempt), but only if the region into which the NP moves is filled with liquid. This evaporation/dragging move is accepted with a different Metropolis probability $P_{acc} = \min[1, \exp(-\beta\Delta H)\frac{n}{\bar{n}}]$, where n is the number of NPs adjacent to cell i_{rnd} and $\bar{n}$ is the number of NPs that are allowed to move. Similarly, reverse moves are included for condensation with the corresponding Metropolis probability, preserving balance.

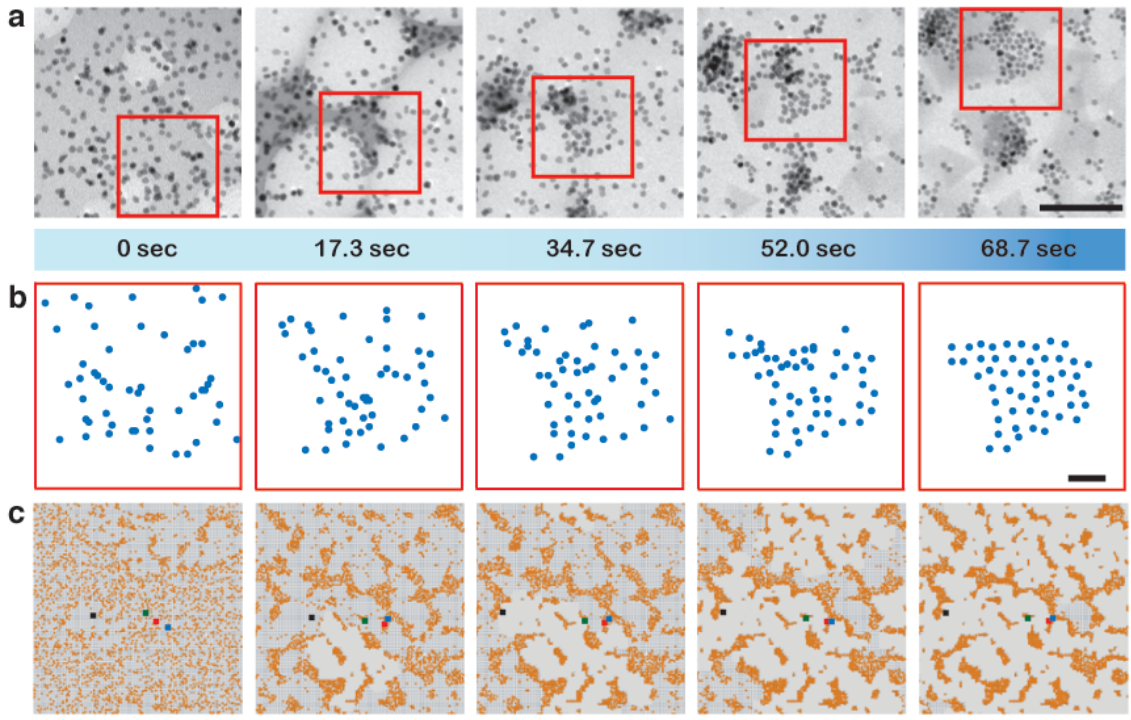

Figure 1: In-situ observation of superlattice formation by liquid phase TEM and lattice gas modeling. (a) TEM snapshots from Movie 1 at different times. The scale bar is 100 nm. (b) Relative positions (corrected for thermal drift of the TEM sample) of selected 51 NPs taken from the red-squared area (120 nm x 120 nm) in Fig. 1a. The scale bar is 20 nm. (c) Top view of assembly formation obtained from lattice gas modeling. Selected NPs are enlarged and colored with black, green, red, and blue to signify their motion Time from left to right correspond to 15000, 25000, 25600, 26400, and 27000 in Monte Carlo (MC) units, respectively for coverage $\rho = 30\%$, chemical potential $\mu = -3\frac{1}{4}\varepsilon_\ell$, temperature $T = \varepsilon_\ell$, and interfacial energies $\varepsilon_{ns} = 1\frac{1}{2}\varepsilon_\ell$, $\varepsilon_{\ell s} = \varepsilon_\ell$, and $\varepsilon_n = 2\varepsilon_\ell$. Image size corresponds to approximately 200×200 nm^2.

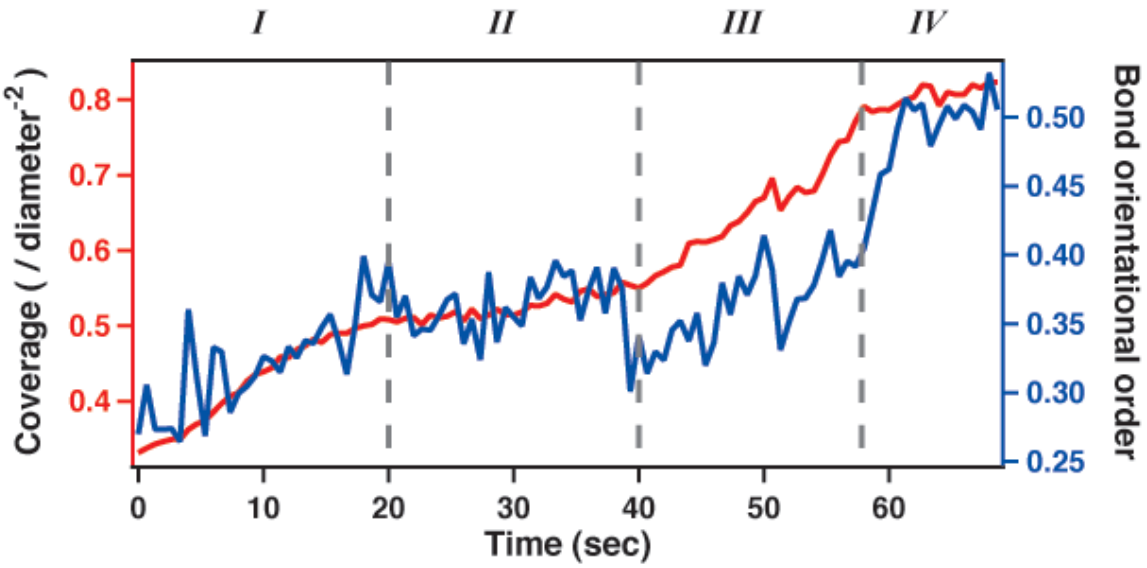

Figure 2: Surface coverage of NPs and the 2D bond orientational order parameter, a measure of crystalline ordering, as a function of time. Results are shown for the same trajectory of Fig. 1b.

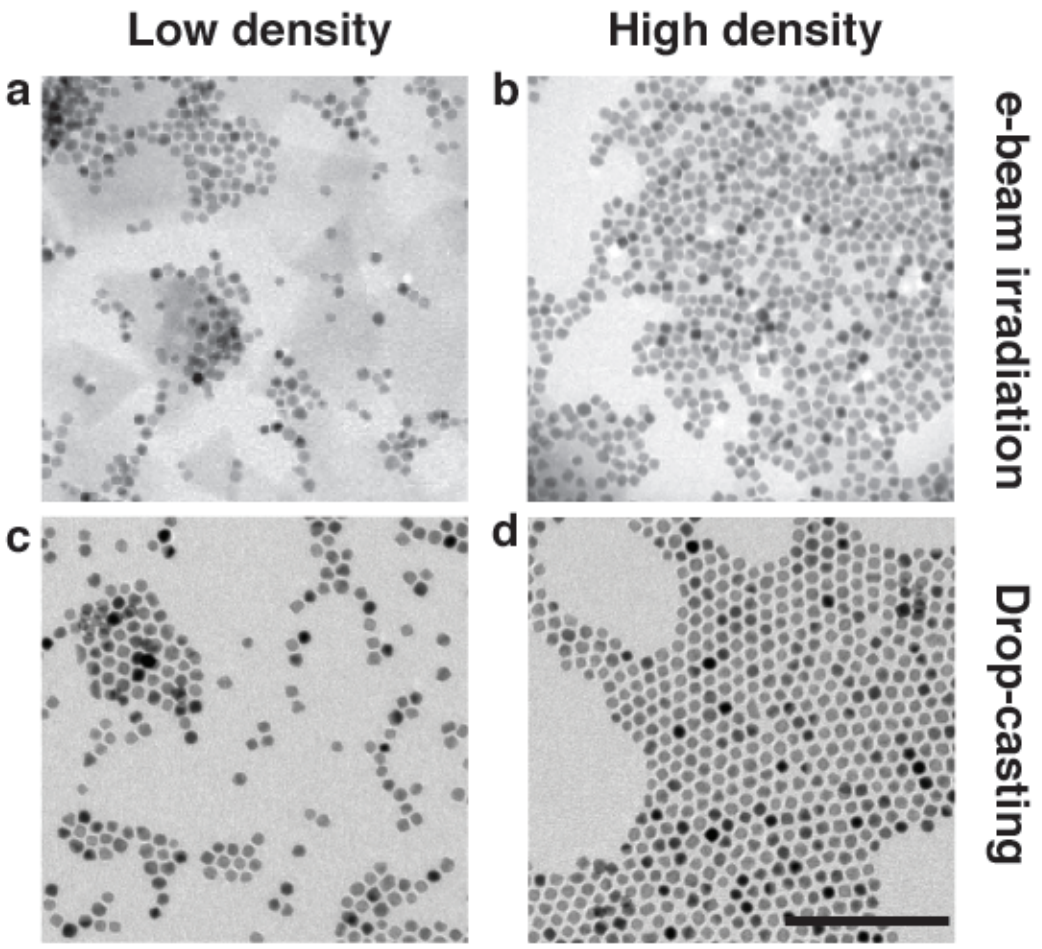

Figure 3: TEM images of NPs assembly formed under electron beam irradiation (panels (a) and (b)) and drop casting (panels (c) and (d)) on SiNx TEM grid. The scale bar is 100 nm.

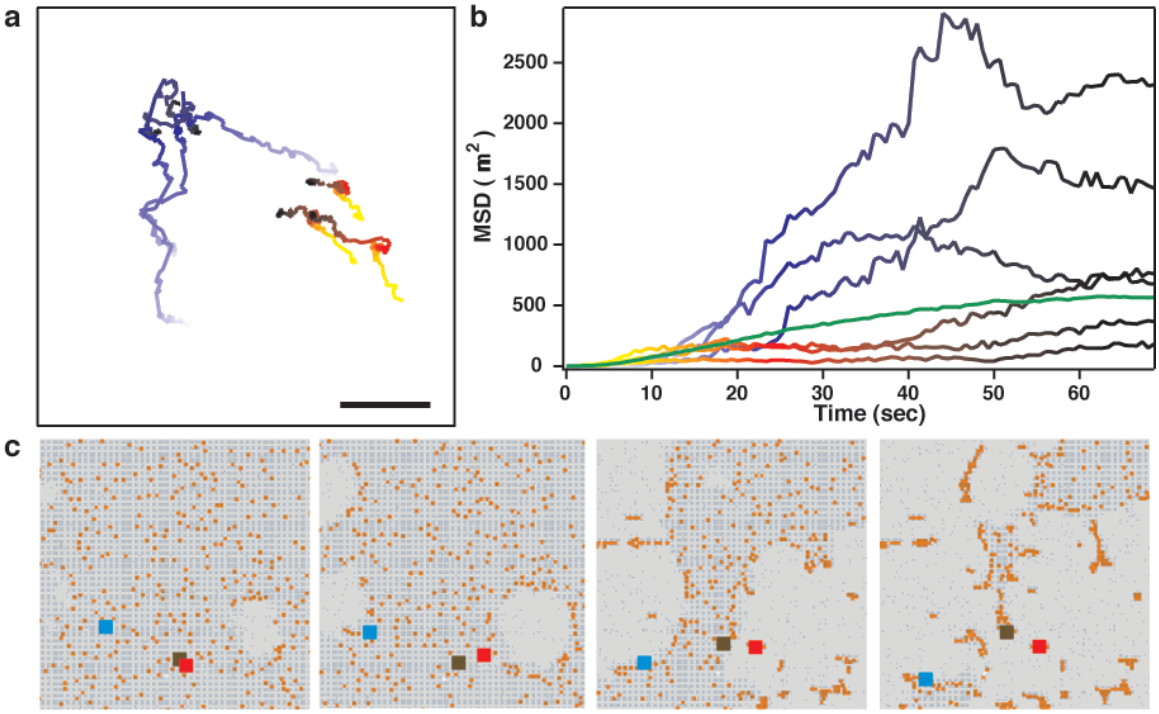

Figure 4: Individual NPs motion in liquid phase TEM observation and lattice gas modeling. (a) Trajectories of selected individual NPs from Fig. 1b for a time step of $\delta t = \frac{1}{3}$ sec. The time variable is labeled with blue and orange color scale for different types of trajectories. Black color indicates final stage of movement. The scale bar is 20 nm. (b) MSD of individual NPs shown in panel (a) with the same color scale along with the average MSD of the selected 51 NPs (green line). (c) Trajectories from lattice gas simulations. Selected NPs are enlarged and colored with red, brown, and blue to signify their motion. Time increases from left to right, for times (in MC steps) 1000, 1200, 1400, and 1600, respectively. Parameters are identical to those in Fig. 1 for a coverage of $\rho = 10\%$, chemical potential $\mu = -3\frac{1}{8}\varepsilon_\ell$, and temperature $T = 2\varepsilon_\ell$. Image size corresponds to approximately 50×50 nm^2.

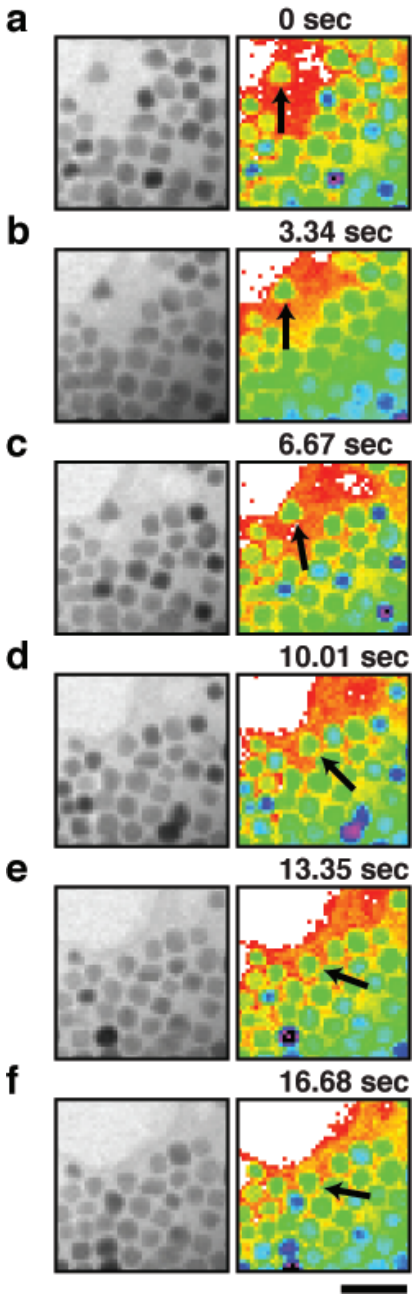

Figure 5: NP addition onto domain of superlattice. (a) – (f) Snapshots from Movie 3 at different times (left frames) and a corresponding color map with rainbow color scale (right frames). Contrast of rainbow color was calibrated such that white color corresponds to dried area. Arrow indicates a NP that moves laterally and rotates until it adequately fills in a vacancy in domain. The scale bar is 25 nm.

References

1 Bishop, K. J. M., Wilmer, C. E., Soh, S. & Grzybowski, B. A. Nanoscale Forces and Their Uses in Self-Assembly. *Small* **5**, 1600-1630 (2009).

2 Baker, J. L., Widmer-Cooper, A., Toney, M. F., Geissler, P. L. & Alivisatos, A. P. Device-Scale Perpendicular Alignment of Colloidal Nanorods. *Nano Lett* **10**, 195-201 (2010).

3 Li, F., Josephson, D. P. & Stein, A. Colloidal Assembly: The Road from Particles to Colloidal Molecules and Crystals. *Angew Chem Int Edit* **50**, 360-388 (2011).

4 Tang, J., Ge, G. L. & Brus, L. E. Gas-liquid-solid phase transition model for two-dimensional nanocrystal self-assembly on graphite. *J Phys Chem B* **106**, 5653-5658 (2002).

5 Anderson, V. J. & Lekkerkerker, H. N. W. Insights into phase transition kinetics from colloid science. *Nature* **416**, 811-815 (2002).

6 Bigioni, T. P. *et al.* Kinetically driven self assembly of highly ordered nanoparticle monolayers. *Nat Mater* **5**, 265-270 (2006).

7 Grzelczak, M., Vermant, J., Furst, E. M. & Liz-Marzan, L. M. Directed Self-Assembly of Nanoparticles. *Acs Nano* **4**, 3591-3605 (2010).

8 Kalsin, A. M. *et al.* Electrostatic self-assembly of binary nanoparticle crystals with a diamond-like lattice. *Science* **312**, 420-424 (2006).

9 Kolny, J., Kornowski, A. & Weller, H. Self-organization of cadmium sulfide and gold nanoparticles by electrostatic interaction. *Nano Lett* **2**, 361-364 (2002).

10 Prasad, B. L. V., Sorensen, C. M. & Klabunde, K. J. Gold nanoparticle superlattices. *Chem Soc Rev* **37**, 1871-1883 (2008).

11 Redl, F. X., Cho, K. S., Murray, C. B. & O'Brien, S. Three-dimensional binary superlattices of magnetic nanocrystals and semiconductor quantum dots. *Nature* **423**, 968-971 (2003).

12 Shevchenko, E. V., Talapin, D. V., Kotov, N. A., O'Brien, S. & Murray, C. B. Structural diversity in binary nanoparticle superlattices. *Nature* **439**, 55-59 (2006).

13 Korgel, B. A., Fullam, S., Connolly, S. & Fitzmaurice, D. Assembly and self-organization of silver nanocrystal superlattices: Ordered "soft spheres". *J Phys Chem B* **102**, 8379-8388 (1998).

14 Rabani, E., Reichman, D. R., Geissler, P. L. & Brus, L. E. Drying-mediated self-assembly of nanoparticles. *Nature* **426**, 271-274 (2003).

15 Denkov, N. D. *et al.* Mechanism of Formation of 2-Dimensional Crystals from Latex-Particles on Substrates. *Langmuir* **8**, 3183-3190 (1992).

16 Gasser, U., Weeks, E. R., Schofield, A., Pusey, P. N. & Weitz, D. A. Real-space imaging of nucleation and growth in colloidal crystallization. *Science* **292**, 258-262 (2001).

17 Grier, D. G. & Murray, C. A. The Microscopic Dynamics of Freezing in Supercooled Colloidal Fluids. *J Chem Phys* **100**, 9088-9095 (1994).

18 Murray, C. A. & Grier, D. G. Video microscopy of monodisperse colloidal systems. *Annu Rev Phys Chem* **47**, 421-462 (1996).

19 Ramos, L., Lubensky, T. C., Dan, N., Nelson, P. & Weitz, D. A. Surfactant-mediated two-dimensional crystallization of colloidal crystals. *Science* **286**, 2325-2328 (1999).

20 Savage, J. R., Blair, D. W., Levine, A. J., Guyer, R. A. & Dinsmore, A. D. Imaging the sublimation dynamics of colloidal crystallites. *Science* **314**, 795-798 (2006).

21 Vanblaaderen, A. & Wiltzius, P. Real-Space Structure of Colloidal Hard-Sphere Glasses. *Science* **270**, 1177-1179 (1995).

22 Abecassis, B., Testard, F. & Spalla, O. Gold nanoparticle superlattice crystallization probed in situ. *Phys Rev Lett* **100**, 115504 (2008).

23 Ge, G. L. & Brus, L. E. Fast surface diffusion of large disk-shaped nanocrystal aggregates. *Nano Lett* **1**, 219-222 (2001).

24 Jiang, Z., Lin, X. M., Sprung, M., Narayanan, S. & Wang, J. Capturing the Crystalline Phase of Two-Dimensional Nanocrystal Superlattices in Action. *Nano Lett* **10**, 799-803 (2010).

25 Lee, B. *et al.* Comparison of Structural Behavior of Nanocrystals in Randomly Packed Films and Long-Range Ordered Superlattices by Time-Resolved Small Angle X-ray Scattering. *J Am Chem Soc* **131**, 16386-16388 (2009).

26 de Jonge, N., Peckys, D. B., Kremers, G. J. & Piston, D. W. Electron microscopy of whole cells in liquid with nanometer resolution. *P Natl Acad Sci USA* **106**, 2159-2164 (2009).

27 Ross, F. M., Williamson, M. J., Tromp, R. M., Vereecken, P. M. & Hull, R. Dynamic microscopy of nanoscale cluster growth at the solid-liquid interface. *Nat Mater* **2**, 532-536 (2003).

28 Zheng, H. M. *et al.* Observation of Single Colloidal Platinum Nanocrystal Growth Trajectories. *Science* **324**, 1309-1312 (2009).

29 Tsung, C. K. *et al.* Sub-10 nm Platinum Nanocrystals with Size and Shape Control: Catalytic Study for Ethylene and Pyrrole Hydrogenation. *J Am Chem Soc* **131**, 5816-5822 (2009).

30 Zheng, H. M., Claridge, S. A., Minor, A. M., Alivisatos, A. P. & Dahmen, U. Nanocrystal Diffusion in a Liquid Thin Film Observed by in Situ Transmission Electron Microscopy. *Nano Lett* **9**, 2460-2465 (2009).

31 Elbaum, M. & Lipson, S. G. How Does a Thin Wetted Film Dry Up. *Phys Rev Lett* **72**, 3562-3565 (1994).

32 Kletenik-Edelman, O. *et al.* Drying-mediated hierarchical self-assembly of nanoparticles: A dynamical coarse-grained approach. *J Phys Chem C* **112**, 4498-4506 (2008).

33 Sztrum, C. G., Hod, O. & Rabani, E. Self-assembly of nanoparticles in three-dimensions: Formation of stalagmites. *J Phys Chem B* **109**, 6741-6747 (2005).

34 Yosef, G. & Rabani, E. Self-assembly of nanoparticles into rings: A lattice-gas model. *J Phys Chem B* **110**, 20965-20972 (2006).

35 Steinhardt, P. J., Nelson, D. R. & Ronchetti, M. Bond-Orientational Order in Liquids and Glasses. *Phys Rev B* **28**, 784-805 (1983).

36 Wang, Z. R., Alsayed, A. M., Yodh, A. G. & Han, Y. L. Two-dimensional freezing criteria for crystallizing colloidal monolayers. *J Chem Phys* **132**, 154501 (2010).

37 Bertozzi, C. R., Chung, S., Shin, S. H. & De Yoreo, J. J. Self-catalyzed growth of S layers via an amorphous-to-crystalline transition limited by folding kinetics. *P Natl Acad Sci USA* **107**, 16536-16541 (2010).

38 Savage, J. R. & Dinsmore, A. D. Experimental Evidence for Two-Step Nucleation in Colloidal Crystallization. *Phys Rev Lett* **102**, 198302 (2009).

39 tenWolde, P. R. & Frenkel, D. Enhancement of protein crystal nucleation by critical density fluctuations. *Science* **277**, 1975-1978 (1997).

40 Vekilov, P. G., Galkin, O., Chen, K., Nagel, R. L. & Hirsch, R. E. Liquid-liquid separation in solutions of normal and sickle cell hemoglobin. *P Natl Acad Sci USA* **99**, 8479-8483 (2002).

41 Sztrum, C. G. & Rabani, E. Out-of-equilibrium self-assembly of binary mixtures of nanoparticles. *Adv Mater* **18**, 565-571 (2006).

42 Egerton, R. F., Li, P. & Malac, M. Radiation damage in the TEM and SEM. *Micron* **35**, 399-409 (2004).

43 Kralchevsky, P. A. & Denkov, N. D. Capillary forces and structuring in layers of colloid particles. *Curr Opin Colloid In* **6**, 383-401 (2001).

Acknowledgements

Work on platinum nanocrystal synthesis, fabrication of liquid TEM cells, and TEM experiment and analysis was supported by the Physical Chemistry of Semiconductor Nanocrystals Program, KC3105, Director, Office of Science, Office of Basic Energy Sciences, of the United States Department of Energy under contract DE-AC02-05CH11231. ER thanks the FP7 Marie Curie IOF project HJSC and the Miller Institute for Basic Research in Science at UC Berkeley for financial support via a Visiting Miller Professorship. HZ thanks the funding support of Laboratory Directed Research Program at Lawrence Berkeley National Lab, funded by the U.S. Department of Energy under Contract No. DE-AC02-05CH11231 for support for her work on liquid cell fabrication and paper revision. We acknowledge the support of National Center for Electron Microscopy, which are funded by the Director, Office of Science, Office of Basic Energy Sciences, Materials Science and Engineering Division of the U.S. Department of Energy under Contract No. DE-AC02-05CH11231. The authors would like to thank David Grauer and Asaph Widmer-Cooper for useful discussion.

Author contributions

J.P. and A.P.A designed this experiment. J.P. synthesized Pt nanoparticles and performed TEM experiments. J.P. and H.Z. fabricated liquid TEM cells. J.P. and W.C.L. carried out analysis of experimental data. P.L.G. and E.R. performed simulation modeling. All authors contributed to the writing and editing of the manuscript.

Additional information

The authors declare no competing financial interests. Supplementary information accompanies this paper on www.nature.com/nmat. Reprints and permissions information is available online at http://npg.nature.com/reprintsandpermissions. Correspondence and requests for materials should be addressed to A.P.A.

DISCLAIMER: This document was prepared as an account of work sponsored by the United States Government. While this document is believed to contain correct information, neither the United States Government nor any agency thereof, nor The Regents of the University of California, nor any of their employees, makes any warranty, express or implied, or assumes any legal responsibility for the accuracy, completeness, or usefulness of any information, apparatus, product, or process disclosed, or represents that its use would not infringe privately owned rights. Reference herein to any specific commercial product, process, or service by its trade name, trademark, manufacturer, or otherwise, does not necessarily constitute or imply its

endorsement, recommendation, or favoring by the United States Government or any agency thereof, or The Regents of the University of California. The views and opinions of authors expressed herein do not necessarily state or reflect those of the United States Government or any agency thereof or The Regents of the University of California.

Supporting information

Direct observation of two-step crystallization in nanoparticle superlattice formation

Jungwon Park[1,2], Haimei Zheng[2], Won Chul Lee[3], Phillip L. Geissler[1,4], Eran Rabani[5], and A. Paul Alivisatos[1,2]*

[1] Department of Chemistry, University of California, Berkeley, CA, 94720, USA

[2] Materials Sciences Division, Lawrence Berkeley National Laboratory, Berkeley, CA, 94720, USA

[3] Department of Mechanical Engineering, University of California, Berkeley, CA, 94720, USA

[4] Chemical Sciences Division, Lawrence Berkeley National Laboratory, Berkeley, CA, 94720, USA

[5] School of Chemistry, The Sackler Faculty of Exact Sciences, Tel Aviv University, Tel Aviv, 69978, Israel

* e-mail: APAlivisatos@lbl.gov

This file includes:

Movie 1, 2, and 3

Materials and methods

Figure S1, S2, S3, S4, and S5

References

1. Movie 1, 2, and 3

Movie 1: In-situ TEM movie for superlattice formation under evaporation of solvent played 5 times faster than real time scale.

Movie 2: Trajectories of selected 51 NPs after correcting thermal drift effect.

Movie 3: In-situ TEM movie for individual NP's addition onto ordered domain played 3 times faster than real time scale.

2. Liquid cell fabrication process and TEM sample preparation

Liquid cell was fabricated based on previously reported procedures by Haimei Zheng *et al.* with controlled thickness of indium spacer which determines the thickness of liquid loaded. Schematic design for liquid cell and fabrication processes can be found in previous reports and Fig. S1.[1,2]

3. NPs tracking method

Recognizing and linking all NPs positions in every time step from TEM movie was not efficient by currently accessible particle tracking algorithms because NPs are overlapped each other while they form dense agglomerates and some NPs are dragged by solvent over the limit that can be detected by algorithm in a given time frame.[3] In addition, non-zero background contrast compared to NPs due to the presence of solvent prohibits efficient detecting process. For image analysis shown

in main manuscript, 51 NPs forming an assembled domain in the final stage were selected from final frame of Movie 1 and tracked in inverse time sequence. Two dimensional position of these selected NPs in different time frames were taken by combination of single-particle tracking method developed for live cell imaging and Image-J software package released by National Institutes of Health. After taking position of NPs with 1/3 sec time interval, center of 51 NPs and their relative positions for each time frame were calculated for the correction of thermal drift effect as follow:

$$(Cx, Cy) = \left(\frac{1}{N}\sum_{i=1}^{N} x_i \ , \frac{1}{N}\sum_{i=1}^{N} y_i \right);\ (Rx_i, Ry_i) = (\ x_i - Cx, y_i - Cy)$$

,where $(x_i, y_i), (Cx, Cy), and\ (Rx_i, Ry_i)$ are original position, center of NPs, and relative position, respectively for N number of NPs. Entire trajectories of 51 NPs obtained from this process are shown in Fig. S1.

4. Lattice gas model

Simulations have been performed in 3D with a lattice gas Hamiltonian defined by:

$$H = -\varepsilon_\ell \sum_{ij} \ell_i \ell_j - \varepsilon_n \sum_{ij} n_i n_j - \varepsilon_{n\ell} \sum_{ij} n_i \ell_j - \varepsilon_{\ell s} \sum_{ij} \ell_i s_j - \varepsilon_{ns} \sum_{ij} n_i s_j - \mu \sum \ell_i,$$

where the sums run only over nearest neighbors on a rectangular 3D lattice, ℓ_i, n_i, and s_j are binary variables roughly proportional to the density of the solvent, nanoparticles and substrate at site i, respectively (0 for low density or 1 for high

density). ε_ℓ, ε_n, $\varepsilon_{n\ell}$, $\varepsilon_{\ell s}$, and ε_{ns} are the liquid-liquid, NP-NP, liquid-NP, liquid-substrate, NP-substrate interfacial energies, respectively.

The specific choice of interaction parameters follows the guidelines described in our previous work. To prevent aggregation of nanoparticles in the presence of the liquid, we take $\varepsilon_\ell < \varepsilon_{n\ell}$. In addition, the attraction between the nanoparticles is taken to be larger than the attraction between the nanoparticles and the liquid, i.e., $\varepsilon_{n\ell} < \varepsilon_n$, so that the nanoparticles tend to aggregate in the absence of liquid. More specifically, we set $\varepsilon_{n\ell} = \frac{3}{2}\varepsilon_\ell$ and $\varepsilon_n = 2\varepsilon_\ell$ in all the results reported in this work.

The last term in the above equation represents the chemical potential, μ, and is used to establish the average concentration of liquid and vapor cells at equilibrium. A large negative value of μ will favor evaporation, while positive values will favor wetting. The crossover from wetting to evaporation occurs at $\mu = -3\varepsilon_\ell$ for the present model. Since the vapor pressure of the nanoparticles and the substrate is negligibly small, we do not include a chemical potential for these species in the Hamiltonian. In other words, the binary variables associated with the nanoparticles and the substrate (n_i and s_i, respectively) conserve the corresponding densities (conserved order parameter), while the binary variable representing the liquid does not conserve density (nonconserved order parameter).

The dynamics are stochastic both for solvent density fluctuations and for NP diffusion, where balance is preserved. The NPs undergo a random walk on the three dimensional lattice, biased by their by their interactions with each other, with liquid cells, and with the substrate. The diffusion rate is controlled by how often we

attempt to displace the nanoparticles compared to the solvent moves (defined below). In detail, we attempt to displace a NP by single lattice spacing in a random direction every N_ℓ solvent moves, but only if the region into which the nanoparticle moves is completely filled with liquid. To maintain solvent density, the void cells left behind the moving nanoparticle are filled with liquid, compensating for the liquid cells overtaken by the nanoparticle in its move. Thus, the nanoparticle moves can be considered as swapping locations between the nanoparticle and the adjacent liquid cells which it displaces. This constraint mimics the very low mobility of nanocrystals on a dry surface. It also provides an additional coupling between the kinetics of evaporation and nanoparticle phase separation. Such a move is accepted with the Metropolis probability:

$$P_{acc} = \min[1, \exp(-\beta \Delta H)],$$

where β is the inverse temperature and ΔH is the energy difference between the new and old configuration. To mimic the low mobility of NPs we choose a large value for N_ℓ (typically 3 orders of magnitude larger than our previous simulations).

In our original work, liquid moves where quite simple. We attempted to convert a randomly chosen lattice cell i that is not occupied by a nanoparticle or the substrate, from liquid to vapor (or from vapor to liquid), $\ell_i \to 1 - \ell_i$ only if at least one of the adjacent lattice cells, j, contains vapor, i.e., if it satisfies $\ell_j + s_j + n_j = 0$). This constraint is applied to both condensation and evaporation to ensure that balance is retained. The direct outcome of this constraint is that evaporation occurs layer by layer (although not necessarily homogeneously for each layer), and the formation of

bubbles (i.e., boiling) is practically never observed. In addition, this constraint also inhibits the formation of configurations, where nanoparticles that are located far from the substrate become surrounded only by vapor cells. The solvent moves are then accepted with the above Metropolis probability, $P_{acc} = \min[1, \exp(-\beta\Delta H)]$.

In the present study, liquid moves are more evolved to include, in a primitive way, "dragging" of the NPs by the receding solvent front. We attempt the same evaporation move described above. However, in addition, if at least one of the neighboring cells is occupied by NPs, we attempt to "drag" the NP in the opposite direction or in the direction of the cell i, depending on whether cell i was filled with liquid or not, respectively, but only if the region into which the NP moves is filled with liquid (as before Solvent density in lattice cells overtaken by this displacement is regenerated in the wake of the moving nanoparticle.). The probability to attempt to drag the NP is given by ξ (for the results described in this work $\xi = 0.001$). In the case that an evaporation move is followed by a dragging move, the Metropolis probability needs to include also the Hastings proposal density:

$$P_{acc} = \begin{cases} \ell_{\mathrm{i}} = 1 & \min[1, \exp(-\beta\Delta H)\frac{n}{\bar{n}}] \\ \ell_{\mathrm{i}} = 0 & \min[1, \exp(-\beta\Delta H)\frac{\bar{n}}{n}] \end{cases},$$

where n is the number of NP adjacent to cell i and $\bar{n}$ the number of NP that are allowed to move.

5. Additional figures

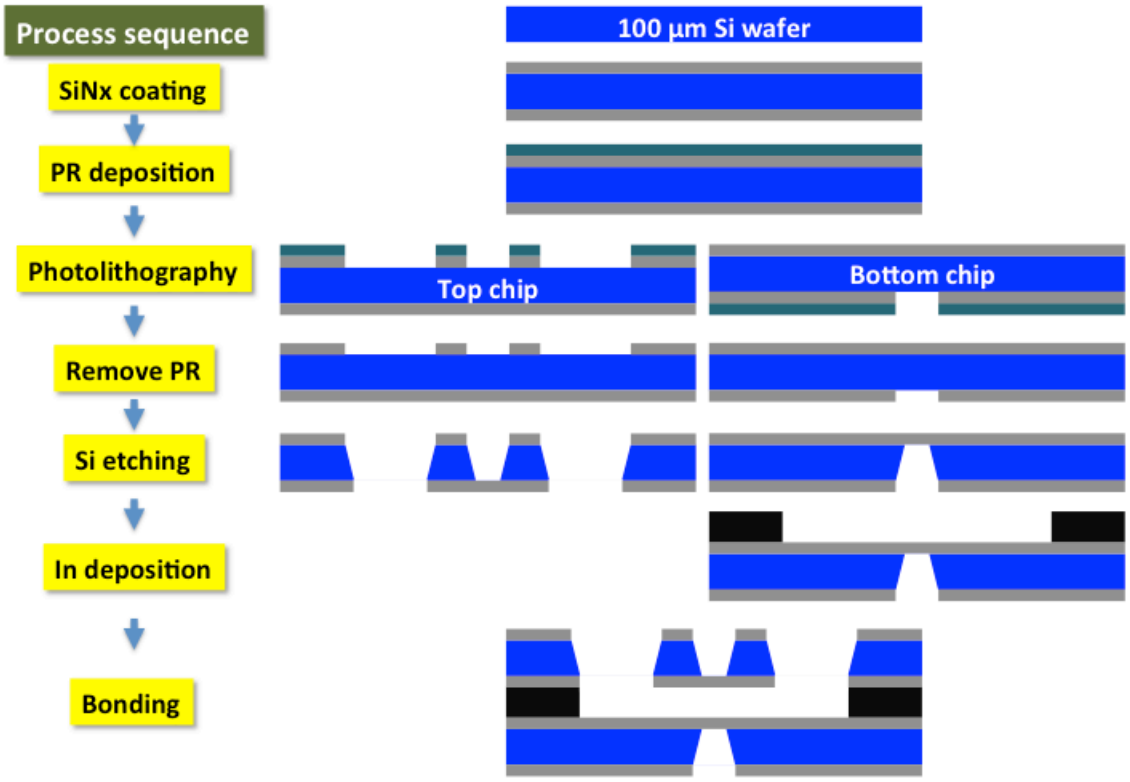

Figure S1: Fabrication process of liquid TEM cell.

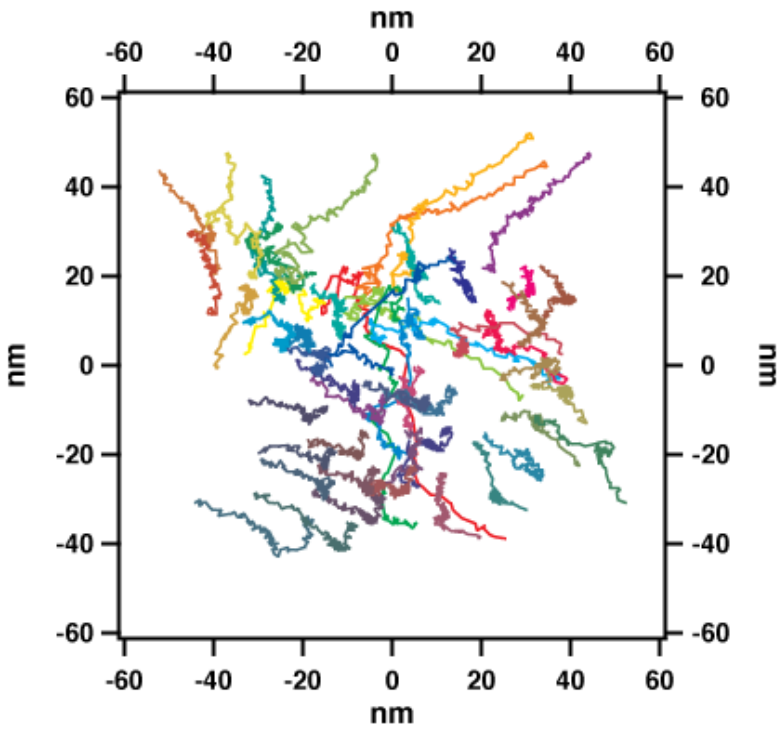

Figure S2: Trajectories of relative position of selected 51 NPs from Movie 1.

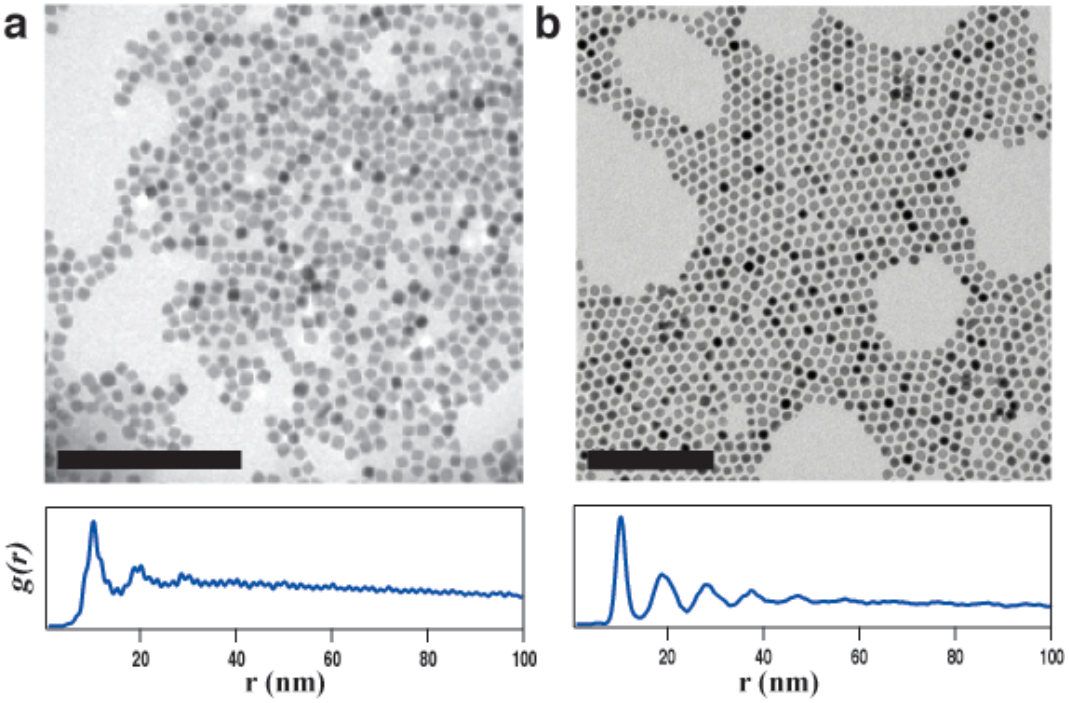

Figure S3: TEM images and and radial-distribution functions of NPs assemblies formed under electron beam irradiation (panels (a)) and drop casting (panels (b))on SiNx TEM grid. The scale bar is 100 nm.

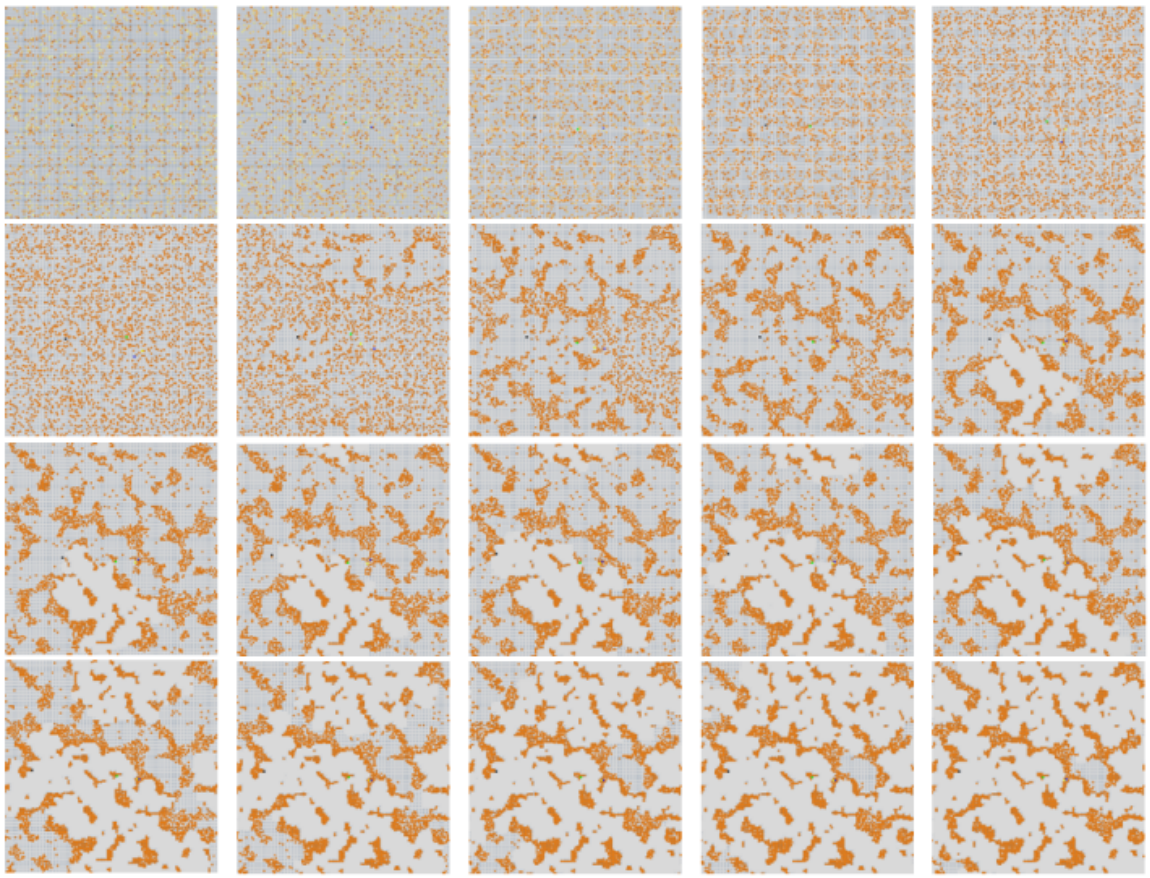

Figure S4: Simulated trajectory showing the full time range from an initial random phase to the assembled phase. Time frames for each image from top left to bottom right are 0, 1000, 2000, 3000, 4000, 10000, 15000, 20000, 22500, 25000, 25200, 25400, 25600, 25800, 26000, 26200, 26400, 26600, 26800, 27000 in MC units, respectively. Darker yellow color indicates NPs closer to substrate. Parameters are specified in the caption of Fig. 1.

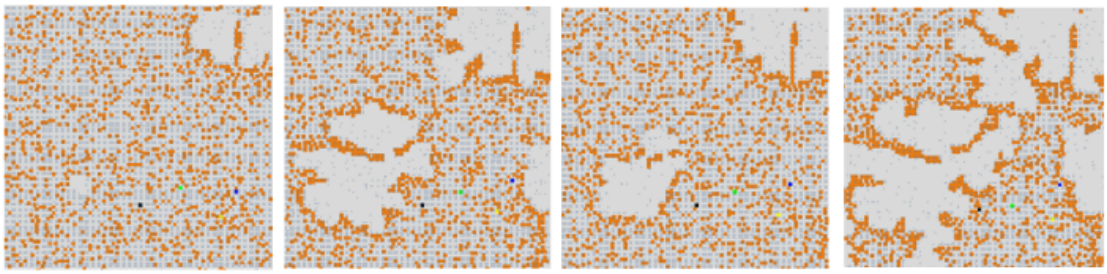

Figure S5: Simulated trajectories showing how NPs are dragged by the solvent front (upper right corner in each image). Time frame from left to right are 900, 1300, 1700, and 2100 in MC steps, respectively. Parameters are identical to those in Fig. 1 with $\mu = -3\frac{1}{4}\varepsilon_\ell$ and $T = 2\varepsilon_\ell$.

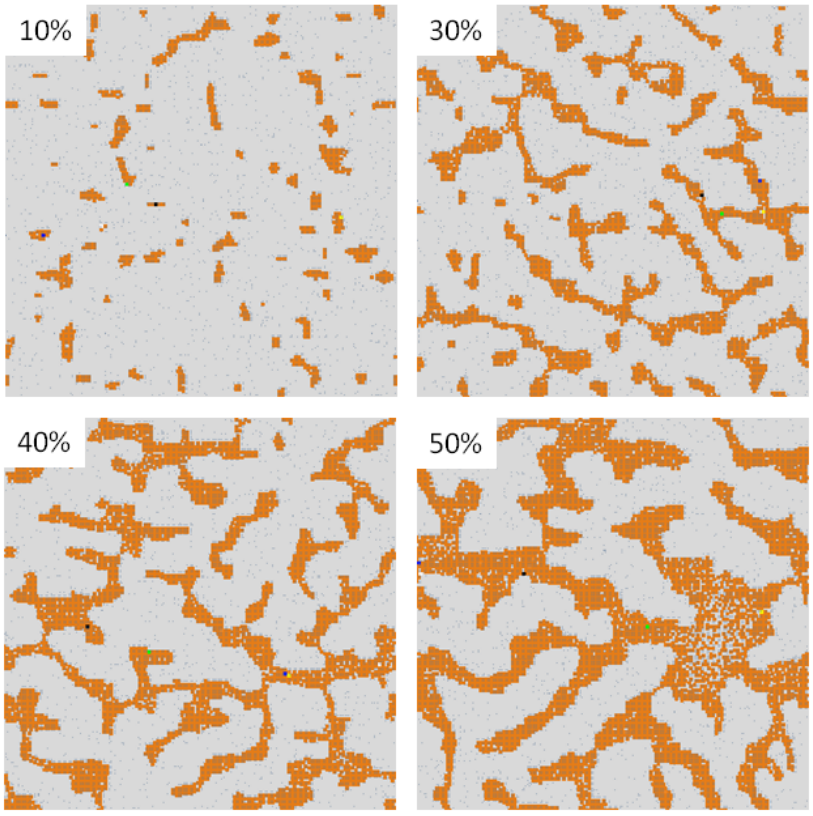

Figure S6: Simulated superlattice patterns with varying coverage of NPs under low NP diffusivity. Parameters are the same as in Fig. 4S.

S1 Zheng, H. M., Claridge, S. A., Minor, A. M., Alivisatos, A. P. & Dahmen, U. Nanocrystal Diffusion in a Liquid Thin Film Observed by in Situ Transmission Electron Microscopy. *Nano Lett* **9**, 2460-2465 (2009).

S2 Zheng, H. M. *et al.* Observation of Single Colloidal Platinum Nanocrystal Growth Trajectories. *Science* **324**, 1309-1312 (2009).

S3 Jaqaman, K. *et al.* Robust single-particle tracking in live-cell time-lapse sequences. *Nat Methods* **5**, 695-702 (2008).